

Hydrogen storage in LiAlH_4 : Predictions of the crystal structures and reaction mechanisms of intermediate phases from quantum mechanics

Jeung Ku Kang and Jai Young Lee

Department of Materials Science and Engineering, KAIST, Daejeon 305-701, Republic of Korea

Richard P. Muller

Computational Materials and Molecular Biology, Sandia National Laboratories, Albuquerque, New Mexico 87185-0996

William A. Goddard III

Materials and Process Simulation Center, California Institute of Technology, Pasadena, California 91125-7400

(Received 23 February 2004; accepted 28 July 2004)

We use the density functional theory and x-ray and neutron diffraction to investigate the crystal structures and reaction mechanisms of intermediate phases likely to be involved in decomposition of the potential hydrogen storage material LiAlH_4 . First, we explore the decomposition mechanism of monoclinic LiAlH_4 into monoclinic Li_3AlH_6 plus face-centered cubic (fcc) Al and hydrogen. We find that this reaction proceeds through a five-step mechanism with an overall activation barrier of 36.9 kcal/mol. The simulated x ray and neutron diffraction patterns from LiAlH_4 and Li_3AlH_6 agree well with experimental data. On the other hand, the alternative decomposition of LiAlH_4 into LiAlH_2 plus H_2 is predicted to be unstable with respect to that through Li_3AlH_6 . Next, we investigate thermal decomposition of Li_3AlH_6 into fcc LiH plus Al and hydrogen, occurring through a four-step mechanism with an activation barrier of 17.4 kcal/mol for the rate-limiting step. In the first and second steps, two Li atoms accept two H atoms from AlH_6 to form the stable Li-H-Li-H complex. Then, two sequential H_2 desorption steps are followed, which eventually result in fcc LiH plus fcc Al and hydrogen: $\text{Li}_3\text{AlH}_6(\text{monoclinic}) \rightarrow 3 \text{LiH}(\text{fcc}) + \text{Al}(\text{fcc}) + 3/2 \text{H}_2$ is endothermic by 15.8 kcal/mol. The dissociation energy of 15.8 kcal/mol per formula unit compares to experimental enthalpies in the range of 9.8–23.9 kcal/mol. Finally, we explore thermal decomposition of LiH, $\text{LiH}(\text{s}) + \text{Al}(\text{s}) \rightarrow \text{LiAl}(\text{s}) + 1/2 \text{H}_2(\text{g})$ is endothermic by 4.6 kcal/mol. The B32 phase, which we predict as the lowest energy structure for LiAl, shows covalent bond characters in the Al-Al direction. Additionally, we determine that transformation of LiH plus Al into LiAlH is unstable with respect to transformation of LiH through LiAl. © 2004 American Institute of Physics.

[DOI: 10.1063/1.1795731]

I. INTRODUCTION

There is great interest in the development of small lightweight hydrogen storage methods^{1,2} for automotive applications. Hydrogen fuel, which can be readily produced from renewable energy sources, contains at least three times larger chemical energy per mass (142 MJ kg^{-1}) than any chemical fuel, thus making a hydrogen fuel cell an attractive alternative to an internal combustion engine for transportation. On the other hand, the problem is how to store it in a small lightweight container. The small lightweight hydrogen storage method may also find its use in a fuel cell system as energy carrier for a portable electronic device.

A hydrogen fuel cell car needs to store at least 4 kg hydrogen to match the range of a gasoline-powered car.¹ To store this amount of hydrogen as hydrogen gas at room temperature and atmospheric pressure requires such a large volume corresponding to a balloon with a 4.5 m diameter that is hardly a practical volume for automotive applications, while a carbon-fiber reinforced high-strength steel container² can fill up as a compressed gas with slightly less than a 60 cm diameter. However, the problem is that the associated risk to

control its accompanying high pressure (450 bars) for this compressed gas exceeds that for gasoline-powered vehicles. To reduce this problem, among the alternatives commercially available today, liquid hydrogen has a good potential of becoming the hydrogen fuel for vehicle transport in that it has a high mass density¹ (70.8 kg m^{-3}) and is also relatively safe. However, despite these advantages, to liquefy hydrogen is cost-expensive and requires an intensive cryogenic process for cooling due to a very low condensation temperature¹ (-252°C at 1 bar) of hydrogen. The additional issue is that the heat transfer through modern available containers for liquid hydrogen can result in loss of up to 40% of the energy content in hydrogen.³ A large container has a smaller surface-to-volume ratio than a small container, thus it is better in reducing heat transfer. However, the condition that a larger hydrogen storage container is better for reducing heat transfer sets a crucial limit to the development of a small hydrogen storage container for liquid hydrogen. Due to these cost-expensive processes and geometric limitation, there has been recently more interest in storing hydrogen on solid state materials such as advanced carbons and light weight metals in-

stead of liquid hydrogen. Dillon *et al.*⁴ reported that 6–8 mass % reversible hydrogen was stored in single-walled nanotubes (SWNTs). However, controversial results^{5,6} have been published concerning true hydrogen storage capacity on advanced carbons. Hirscher and co-workers⁵ argued against the report of Dillon *et al.* by showing that titanium hydrides in the SWNT stored large amounts of hydrogen, but hydrogen storage capacity on SWNT itself was less than 1 mass %. Likewise, Chen *et al.*⁶ also showed that the increase in hydrogen storage capacity by alkaline metal-doped carbon NTs was attributed to formation of metal hydrides. Although these results are not confirmative, putting all these results together one could say that the adsorbed reversible hydrogen on tubular forms of carbon is still not satisfying the United States Department of Energy (DOE) target¹ of 6.5 mass % set for automotive applications.

The promising alternative for hydrogen storage is a metal hydride system. Metal is capable of absorbing large amounts of hydrogen while releasing heat as it is filled with hydrogen under a moderate pressure and then releases hydrogen as reducing the pressure or supplying the heat it needs. However, there are considerable challenges to meet the requirements for vehicular applications, which include: (1) increasing the maximum weight percent of reversibly adsorbed hydrogen to 6.5% more,¹ (2) increasing the maximum hydrogen capacity per volume to 62 kg m⁻³ more,¹ and (3) improving the rate for adsorption/desorption to peak consumption of 1–3 g s⁻¹.⁷ These are all important, but no metal hydride system has been found to meet all these demands. There are many reaction steps that may hinder kinetically a metal hydride system to reach its thermodynamic equilibrium of hydrogen storage within a reasonable time. For example, although magnesium-based metal hydrides can store up to 7.6 mass % hydrogen,⁸ they exhibit kinetics too slow for practical applications. Consequently, it is currently essential to find materials exhibiting high volumetric/gravimetric hydrogen capacity in combination with enhanced kinetics at modest temperatures.

One system of technological interest is the LiAlH₄ system. The maximum available weight percentage and the hydrogen capacity per volume are 10.6 wt. % and 96 kg m⁻³, respectively. Chen *et al.*⁹ recently showed that titanium chloride-doped LiAlH₄ lowered the decomposition temperature of LiAlH₄, which resulted from the enhanced kinetics for a dehydriding cycle. Thus development of catalysts for the enhanced kinetics of LiAlH₄ is very attractive since it can eliminate the need for high temperature and high pressure previously required for the rehydriding/dehydriding cycle.

Vajeeston and other co-workers^{10,11} have recently studied a detailed high-pressure-induced transformation of LiAlH₄ and Li₃AlH₆ using the *ab initio* project plane-wave method.¹² At 33.8 GPa, they predicted that the phase transition from monoclinic LiAlH₄ to orthorhombic LiAlH₄ can occur, while Li₃AlH₆ stabilizes in space group *R*-3 at ambient pressure. However, despite these detailed studies and the promise of lithium aluminum hydride systems, there remain still considerable challenges in optimizing these systems, which are impeded by the uncertainties about thermody-

namics and kinetic parameters of removing hydrogen from them and adding hydrogen to them. In addition there remain uncertainties about thermal behaviors of crystal structures, atomic configurations, and electronic structures for various intermediate phases likely to be involved in hydrogen storage as the temperature changes. Thus we initiated a series of first-principles density functional theory^{13,14} calculations to determine the temperature-induced decomposition mechanisms, and thermodynamic and kinetic parameters of various intermediate phases for hydrogen storage in LiAlH₄. These results are reported here in Sec. III. Section II provides some details about the calculations while Sec. IV summarizes our results and discusses points that remain to be clarified.

II. COMPUTATIONAL DETAILS

All calculations are performed using the PW91 (Ref. 15) and KMLYP (Ref. 16) methods. The Li and Al atoms are described using non-local norm-conserving Vanderbilt scalar pseudopotentials¹⁷ to replace the 1s electrons of Li and the Ne core of Al. The set of *k* points used to expand the molecular wave function is based on the Monkhorst-Pack scheme.¹⁸ To overcome problems associated with finite *k*-point sampling in metallic systems, we use the thermal broadening scheme¹⁹ of Gillan with broadening energies of 0.2 eV.

We use a plane-wave basis, but truncated to include only plane waves having kinetic energies <270 eV. To test the adequacy of using this cutoff we first consider the B32 (space group *Fd*-3*m*) structure for LiAl and perform the total energy calculations using the 9880 *k* points corresponding to the 270 eV cutoff energy and the 37 671 *k* points corresponding to a 300 eV cutoff energy. The total energies per formula unit differ by only 0.6 kcal/mol. Likewise, for fcc Al the difference between energies obtained with these two cutoff energies is <0.2 kcal/mol. These results suggest that the 270 eV cutoff energy is somehow optimal in terms of being able to reduce significantly the considerably expensive computational cost and also to reproduce well total energies for the systems of Li and Al elements upon using much larger cutoff energies. Consequently, we use a cutoff energy of 270 eV for all of the calculations reported herein.

Unless otherwise noted all energies are corrected for the zero-point energy (ZPE), which are calculated at the geometries obtained through full optimization. All electronic structure calculations for optimizing geometries are performed with the CASTEP (Ref. 20) program while vibration frequencies are obtained using the DMO13 (Ref. 21) program using the DN (DN—double-numeric) quality basis set. On the other hand, to determine the activation barriers for decomposition of LiAlH₄ and Li₃AlH₆ we perform geometry optimizations and frequency calculations using the GAUSSIAN04 package,²² where the electronic wave functions are expanded using the 6-31+(*d*,*p*) (Ref. 23) diffuse double-zeta plus polarization basis set. In addition x-ray diffraction (XRD) (Ref. 24) using a Cu radiation of 1.542 Å and neutron diffraction (ND) (Ref. 25) using a neutron source of 1.555 Å are simulated to obtain *d* spacing, 2θ, and intensities for *hkl* reflections.

TABLE I. Summary of reaction energies per formula unit from this work and experiments.

Reaction	This work (kcal/mol)	Experiment (kcal/mol)
Thermal decomposition of monoclinic LiAlH ₄		
$\text{LiAlH}_4^a \rightarrow 1/3\text{Li}_3\text{AlH}_6^b + 2/3\text{Al}^c + \text{H}_2^d$	14.1 ⁱ (6.9 ^j)	6.6 ^k
$\text{LiAlH}_4^a \rightarrow \text{LiAlH}_2^c + \text{H}_2^d$	17.4 ⁱ	
Thermal decomposition of monoclinic Li ₃ AlH ₆		
$\text{Li}_3\text{AlH}_6^b \rightarrow 3\text{LiH}^c + \text{Al}^c + 3/2\text{H}_2^d$	15.8 ⁱ	9.8 ^l , 23.9 ^m
$\text{Li}_3\text{AlH}_6^b + 2\text{Al}^c \rightarrow 3\text{LiAlH}^g + 3/2\text{H}_2^d$	57.2 ⁱ	
Thermal decomposition of LiH		
$\text{LiH}^f + \text{Al}^c \rightarrow \text{LiAl}^b + 1/2\text{H}_2^d$	4.6 ⁱ	
$\text{LiH}^f + \text{Al}^c \rightarrow \text{LiAlH}^g$	13.8 ⁱ	

^aMonoclinic phase of space group $P2_1/c$ (No. 14) used and zero-point corrections is 20.10 kcal/mol.

^bMonoclinic phase of space group $P2/m$ (No. 12) used and zero-point corrections is 32.19 kcal/mol.

^cFace-centered cubic lattice used and zero-point corrections is 0.66 kcal/mol.

^dZero-point corrections of 6.24 kcal/mol.

^eTriclinic phase used.

^fFace-centered-cubic lattice structure used.

^gTriclinic phase and no zero-point corrections used. This phase is a modified structure of B32 LiAl.

^hB32 structure (space group No. 227) and zero-point corrections of 1.22 kcal/mol used.

ⁱReaction energy calculated without zero-point and thermal corrections.

^jGibbs free energy change estimated at 298 K.

^kGibbs free energy change at 298 K from Ref. 31.

^lEnthalpy change from 373.15 K to 448.15 K from Ref. 9.

III. RESULTS AND DISCUSSION

We calculate the structures and energies for a number of alternative crystal structures for each compound: LiAl, LiAlH₄, Li₃AlH₆, LiAlH₂, LiAlH, LiH, and Al. In each case we use a supercell to allow the structure to adopt unexpected structures.

A. LiAl

First, we perform full optimizations to determine the crystal structures for six different LiAl phases, namely, the $Fd-3m$ (B32), $Pm-3m$ (B2), $P4/mmm$ (L1₀), $Pnma$ (B27), $P6_3mc$ (B4), and $P2_1/c$ space group types, where B32, B2, L1₀, B27, and B4 represent “Pearson” symbols. EPAPS (Ref. 26) (see Table I) summarizes their predicted lattice parameters, atomic positions, and energies per formula unit. We find that the lowest energy structure for LiAl is higher for the B32 phase, with the L1₀ phase 9.8 kcal/mol, the B27 phase 13.4 kcal/mol, the monoclinic ($P2_1/c$) phase 16.4 kcal/mol, the B2 phase 19.8 kcal/mol, and the B4 phase 38.7 kcal/mol.

B32 is a NaTl type structure based on a body-centered-cubic (bcc) lattice as shown in Fig. 1(a), but in which each Al has four Al neighbors tetrahedrally coordinated and four Li neighbors also tetrahedrally coordinated. In addition each Li has the same environment. We find that the Al-Al bond charge (see Fig. 2) is more localized in the Al-Al direction, suggesting covalent Al-Al (2.70 Å) bonds, but there is a uniform electron density in the Li-Li and Al-Li direction, suggesting metallic bonding. Thus one can visualize the B32 structure as a mixture of covalent bonding for the Al-Al bonds and of metallic bonding in the Li-Li direction. The Al-Al distance here of 2.70 Å is shorter than 2.82 Å for the bulk metal fcc Al, suggesting stronger bonding between Al atoms than that for fcc Al. Our calculated equilibrium lattice of 6.23 Å compares with the experimental result²⁷ of 6.36 Å. The difference between theory and experiment is attributed to thermal expansion of lattice at an experimental temperature.

Figure 1(b) shows the B2 structure, which is a CsCl type structure with a simple bcc lattice with each Al coordinated to eight Li and each Li coordinated to eight Al. The eight nearest neighbors to the Al are Li atoms and it has the Al-Li

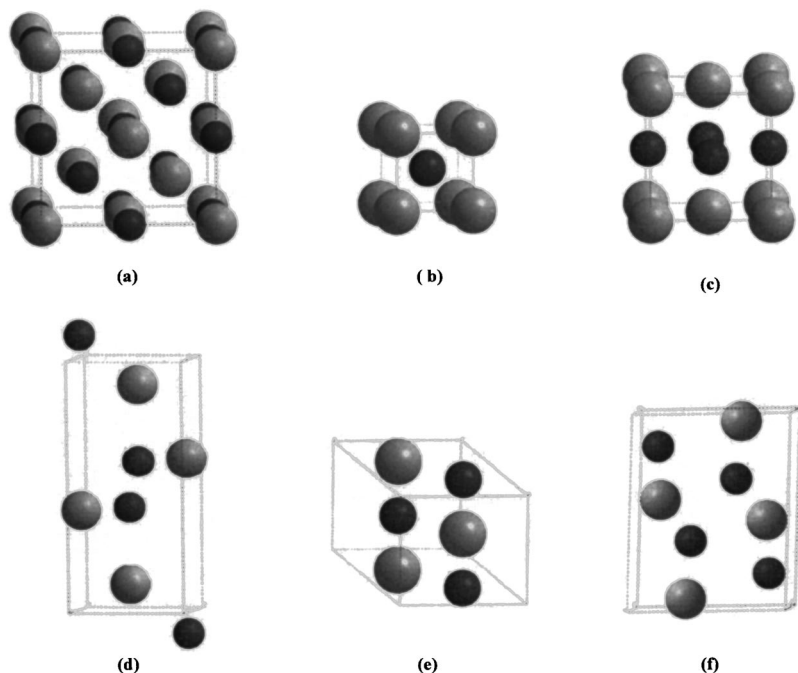


FIG. 1. Optimized structures for six different LiAl phases: (a) $Fd-3m$ (B32), (b) $Pm-3m$ (B2), (c) $P4/mmm$ (L1₀), (d) $Pnma$ (B27), (e) $P6_3mc$ (B4), and (f) $P2_1/c$ space group types. Li atoms are shown in gray while Al atoms are shown in dark gray.

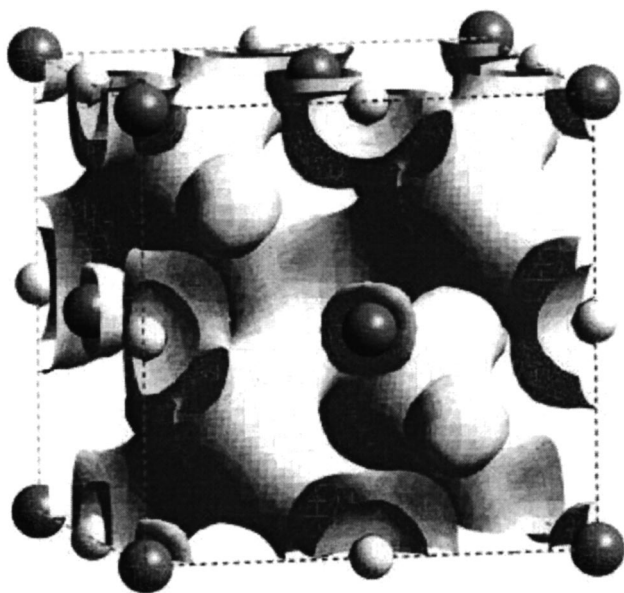


FIG. 2. The charge density distribution for B32 LiAl, where was created with an isosurface value of 0.18. Li atoms are shown in dark gray while Al atoms are shown in white.

distances of 2.67 Å shorter than the 2.70 Å for Al-Li bonds of B32. On the other hand, the Al-Al distances of 3.09 Å to the six second-nearest neighboring Al atoms are much larger than the 2.70 Å for the B32 structure or the 2.82 Å for fcc Al. The density for the B2 phase is higher than that for B32 LiAl. These results suggest the following simple picture for the bonding in the B2 structure. The Al atoms in the B2 structure would like to form stronger bonds by coming closer together, but the pressure of the electrons provided by the Li atoms counteracts this tendency. Upon applying sufficient pressure, the Al-Al bonding becomes sufficiently strong to make the B2 structure the most stable. We find that above 15.0 G bars the B2 structure is more stable than B32, which compares to the theoretical estimate of 1.4 G bars by Guo, Podlucky, and Freeman.²⁸ At this phase transition we find that the lattice parameter decreases by 6.8%.

Li_0 is a CuAu type structure based on fcc lattice as shown in Fig. 1(c). Each Al has four nearest neighbors Al atoms in a plane plus eight Li atoms out of this plane. The Al-Al distances of 2.75 Å are shorter than the 2.82 Å for fcc Al, but slightly >2.70 Å for the B32 structure. Thus we consider that the Al-Al bond is weaker than the tetrahedral bond for B32. In addition the plane arrangement of Al atoms in Li_0 is less favorable for the sp^3 hybrids needed to form localized covalent bonds in the B32 structure.

Figure 1(d) shows the optimized geometries for $Pnma$ LiAl. This phase is based on an orthorhombic lattice in which each Al is coordinated to the first nearest two Al atoms, the second nearest two Li atoms, and the third nearest five Li atoms. This structure (space group of No. 62) is predicted to have the lattice parameters

$$a=9.53 \text{ Å}, \quad b=3.94 \text{ Å}, \quad c=4.26 \text{ Å}$$

$$\text{with } \alpha=\beta=\gamma=90.0^\circ.$$

The Al-Al distances of 2.54 Å shows more strong Al-Al bond characters in this orthorhombic phase than B32, but the bond angles of 101.4° for Al-Al-Al indicates that they are somehow in angular distortions. In addition the Al-Li distances of 2.82 Å to 2.91 Å compare to the 3.02 Å for fcc Li.

$P6_3mc$ LiAl is a ZnO type structure based on a hexagonal lattice as shown Fig. 1(e) in which alternating Al and Li atoms are coordinated to form a complete hexagonal cyclic ring as in the case of graphite. The Al-Li bond distance on the basal plane is 2.88 Å while the bond distance between Li and Al (two) along the c -axis direction is 2.49 Å. In addition the bond angle for Li-Al-Li, where two Li and one Al are on the basal plane, is 120.0° while the other bond angle for Li-Al-Li, where one Li and one Al are on the basal plane and the other Li atom is along the c axis, is 90.0° . This structure, which belongs to space group of No. 186, has predicted lattice parameters

$$a=b=4.99 \text{ Å}, \quad c=4.98 \text{ Å}$$

$$\text{with } \alpha=\beta=90.0^\circ, \quad \gamma=120.0^\circ.$$

The more details for atomic positions are also given in EPAPS (see Table I).

Figure 1(f) shows the $P2_1/c$ LiAl structure based on a monoclinic lattice. Each Al is coordinated to the first nearest four Li and to the second nearest four Al. However, some amounts of bond and angular distortions under this symmetry make it impossible to form a complete tetrahedral coordination. Our calculated lattice parameters are given,

$$a=4.50 \text{ Å}, \quad b=7.25 \text{ Å}, \quad c=7.90 \text{ Å}$$

$$\text{with } \alpha=\gamma=90.0^\circ, \quad \beta=138.0^\circ.$$

Atomic positions for Al and Li atoms in the primitive cell are also given in Table I on EPAPS. We find that the Al-Al bonds have significantly elongated bond lengths of 3.2–4.1 Å and their bond angles distorted from 109.5° also indicate a certain amount of angular strain.

B. LiAlH_4

LiAlH_4 consist of AlH_4^- anions (the H atoms are tetrahedrally coordinated around the Al atom) spaced by Li^+ counter ions. Recently Hauback, Brinks, and Fjellvåg²⁹ proposed atomic positional parameters for monoclinic LiAlD_4 (space group $P2_1/c$) using combined synchrotron x-ray and neutron diffraction. Their proposed lattice parameters at 295 K are

$$a=4.8 \text{ Å}, \quad b=7.8 \text{ Å}, \quad c=7.9 \text{ Å}$$

$$\text{with } \alpha=90.0^\circ, \quad \beta=112.3^\circ, \quad \gamma=90.0^\circ.$$

This value compares to the other x-ray experimental result obtained from monoclinic LiAlH_4 by Chen *et al.*,⁹ which was identified by comparing their x-ray hkl reflections to JCPDS files (12-473) from ICDD (International Center for Diffraction Data):

$$a=4.8 \text{ Å}, \quad b=7.9 \text{ Å}, \quad c=7.9 \text{ Å}$$

$$\text{with } \alpha=90.0^\circ, \quad \beta=111.5^\circ, \quad \gamma=90.0^\circ.$$

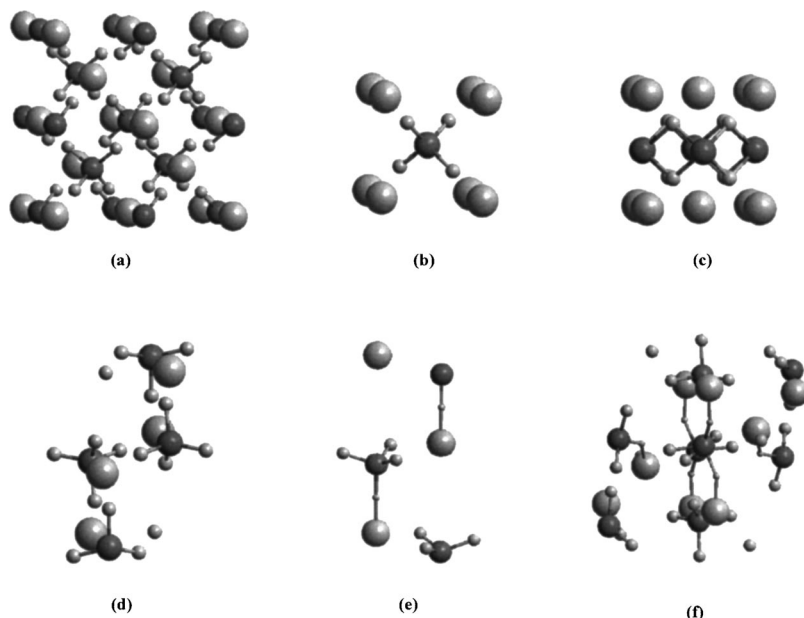


FIG. 3. Optimized structures for six different LiAlH_4 phases: (a) $Fd-3m$ (B32), (b) $Pm-3m$ (B2), (c) $P4/mmm$ ($L1_0$), (d) $Pnma$ (B27), (e) $P6_3mc$ (B4), and (f) $P2_1/c$ types. Li and H atoms in gray are shown in large and small spheres, respectively, while Al atoms are shown in dark gray.

However, the atomic positional parameters and structural stabilities for other phases of LiAlH_4 have not been known yet. Thus we determine atomic positions and energetics for various phases of LiAlH_4 through full optimizations of geometries. In addition XRD and neutron diffraction peaks are simulated at these optimized structures of LiAlH_4 to compare with experimental results.

As an initial guess for the structure of LiAlH_4 we modified the B32 LiAl type structure as shown in Fig. 3(a) in which each Al is replaced with an AlH_4 unit. The full geometry optimization for this structure leads to lattice parameters:

$$a = 8.11 \text{ \AA}, \quad b = 8.11 \text{ \AA}, \quad c = 8.11 \text{ \AA},$$

$$\text{with } \alpha = 90.0^\circ, \quad \beta = 90.0^\circ, \quad \gamma = 90.0^\circ.$$

These predicted lattice parameters and volume density of 0.947 g cm^{-3} compare to the experimental lattice parameters

and the volume density of 0.905 g cm^{-3} . The predicted atomic positions for this optimized structure are given in EPAPS (Table II), where each Al has the nearest four H in a tetrahedral coordination to form AlH_4^- with the Al-H bond lengths of 1.61 \AA and the Li-H bond lengths of 1.94 \AA . On the other hand, we find that the simulated XRD and ND from this B32 phase disagree with the experimental hkl reflections.^{9,29}

Next, we determine the atomic positions for the B2 LiAlH_4 phase [see Fig. 3(b)], but find that it does not reproduce experimental hkl reflections. Thus we search for other structure types for LiAlH_4 to find the structure consistent with the experimental hkl reflections. We find that the simulated XRD and ND [see Figs. 4(a) and 4(b)] from monoclinic LiAlH_4 of space group $P2_1/c$, agree well with the experimental patterns. As the geometry for simulating hkl reflections, we use the structure fully optimized using a supercell

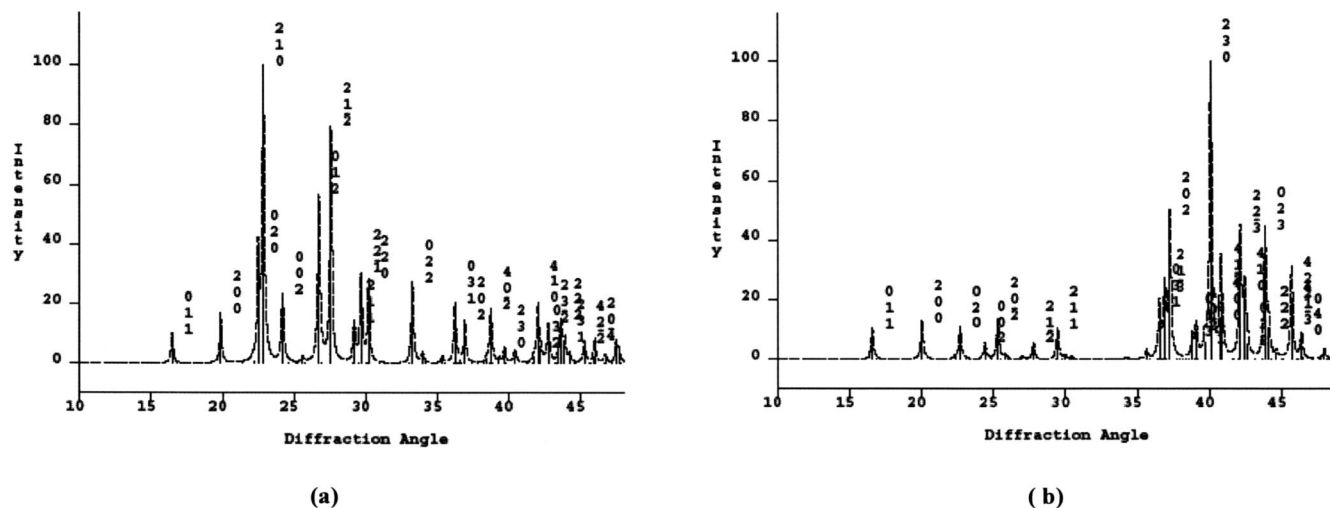


FIG. 4. Simulated x-ray diffraction and neutron diffraction from $P2_1/c$ LiAlH_4 using a Cu radiation of 1.542 \AA and a neutron source of 1.555 \AA , respectively: (a) XRD and (b) ND. Diffraction angles are 2θ values.

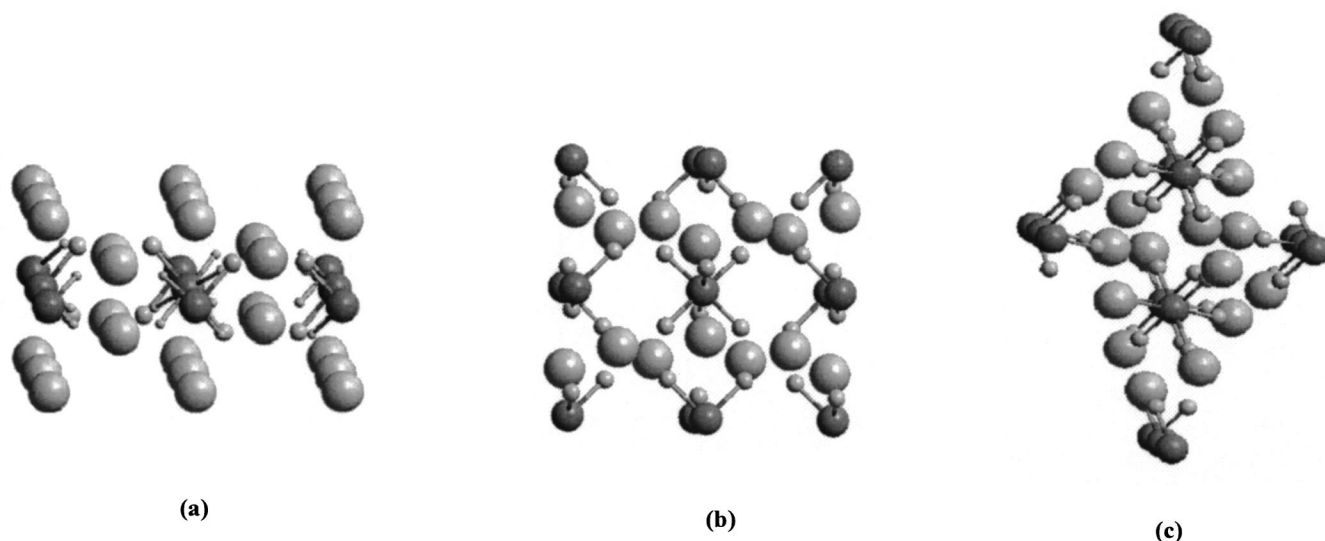


FIG. 5. Optimized structures for Li_3AlH_6 phases of three different symmetries: (a) $P2_1/m$ (No. 11), (b) $P2/m$ (No. 12), and (c) $R-3$ (No. 148) types. Li and H atoms in gray are in large and small spheres, respectively, while Al atoms are shown in dark gray.

twice as large as the size for the primitive cell. The strongest XRD peak is (210) and the ratio to the second strongest peak is $I(21-2)/I(210)=89.03\%$, while the third strongest peak leads to $I(012)/I(210)=63.93\%$, as shown in EPAPS (Table III). Likewise, the more details from simulated powder neutron diffraction, including d spacing, neutron 2θ , and intensity, are also summarized in Table III on EPAPS, where the strongest peak is (230) while the ratio to the second strongest peak is $I(202)/I(230)=50.10\%$. This monoclinic structure is a modification of the monoclinic LiAl structure and denoted as $P2_1/c \text{ LiAlH}_4$, which is predicted to have lattice parameters

$$a=4.8 \text{ \AA}, \quad b=7.6 \text{ \AA}, \quad c=7.8 \text{ \AA}$$

$$\text{with } \alpha=90.0^\circ, \quad \beta=110.6^\circ, \quad \gamma=90.0^\circ.$$

These parameters are in a close agreement with experimental results^{9,29} and theoretical results.¹⁰ The atomic positions are also given in EPAPS (see Table II), in which each Al has four H tetrahedrally coordinated to form AlH_4^- that has three Al-H bond lengths of 1.60 Å and one Al-H bond length of 1.62 Å. On the other hand, Li^+ is ionic bound to AlH_4^- , where the distance between Li-H is 1.89–1.92 Å. In addition the predicted band gap of 4.6 eV indicates that this hydride is an insulator.

Figure 3(c) shows the LiAlH_4 structure of space group $L1_0$. The predicted lattice parameters and atomic positions for this $L1_0$ phase are summarized in EPAPS (Table II). Each Al has eight H octahedrally coordinated with the Al-H bond lengths of 1.85 Å while the Li-H bond distances are 1.91 Å. On the other hand, we find that the total energy per formula unit is 30.7 kcal/mol higher than that for $P2_1/c$.

EPAPS (Table II) summarizes the optimized geometries and atomic positions from orthorhombic (space group of No. 62) LiAlH_4 [see Fig. 3(d)] in which each Al has four H tetrahedrally coordinated to form a stable complex of AlH_4^- with Al-H bond lengths of 1.59–1.61 Å. However, we find that the total energy is 8.8 kcal/mol per formula unit higher

than that for $P2_1/c \text{ LiAlH}_4$. In addition the simulated XRD and ND patterns from this structure are not consistent with experimental results.

Finally, we calculate the atomic positions for H, Li, and Al atoms in the hexagonal structure [see Fig. 3(e)], and the results are summarized in EPAPS (Table II). Each Al has four H tetrahedrally coordinated, which forms the complexes of AlH_4^- with Al-H bond lengths of 1.60–1.61 Å. On the other hand, Li^+ is ionic bound to AlH_4^- , where the Li-H distance is 1.73 Å. The total energy per formula unit is higher by only 3.7 kcal/mol than that for the orthorhombic structure. Therefore, we expect that the hexagonal structure can transform to the orthorhombic structures at a moderate condition. When going from the hexagonal structure to the orthorhombic structure, the structure preserves the wurtzite type arrangements of the $(\text{AlH}_4)^-$ and Li^+ ions during the phase transformation and it expands along hexagonal c (orthorhombic a) and contracts in the basal plane.

C. Li_3AlH_6

The Li_3AlH_6 structure is described in terms of three Li^+ molecules surrounding each $[\text{AlH}_6]^{-3}$ molecule. First, we search for the structure consistent with the experimental XRD data⁹ [ICDD (Li_3AlH_6), 27-282]] and find that the simulated XRD patterns (Table V on EPAPS) from monoclinic structure of space group $P2/m$ as shown in Fig. 5(b) are in a close agreement with experimental result. The predicted strongest two reflections are (111) with $2\theta=21.53^\circ$ and (11-1) with $2\theta=21.53^\circ$ and $I(11-1)/I(111)=75.5\%$ while the third strongest peak is (020) with $2\theta=21.28^\circ$ and $I(020)/I(111)=50.05\%$. The optimized structure has lattice parameters

$$a=8.0 \text{ \AA}, \quad b=8.3 \text{ \AA}, \quad c=5.7 \text{ \AA}$$

$$\text{with } \alpha=90.0^\circ, \quad \beta=93.4^\circ, \quad \gamma=90.0^\circ,$$

$$\rho=0.949 \text{ g cm}^{-3},$$

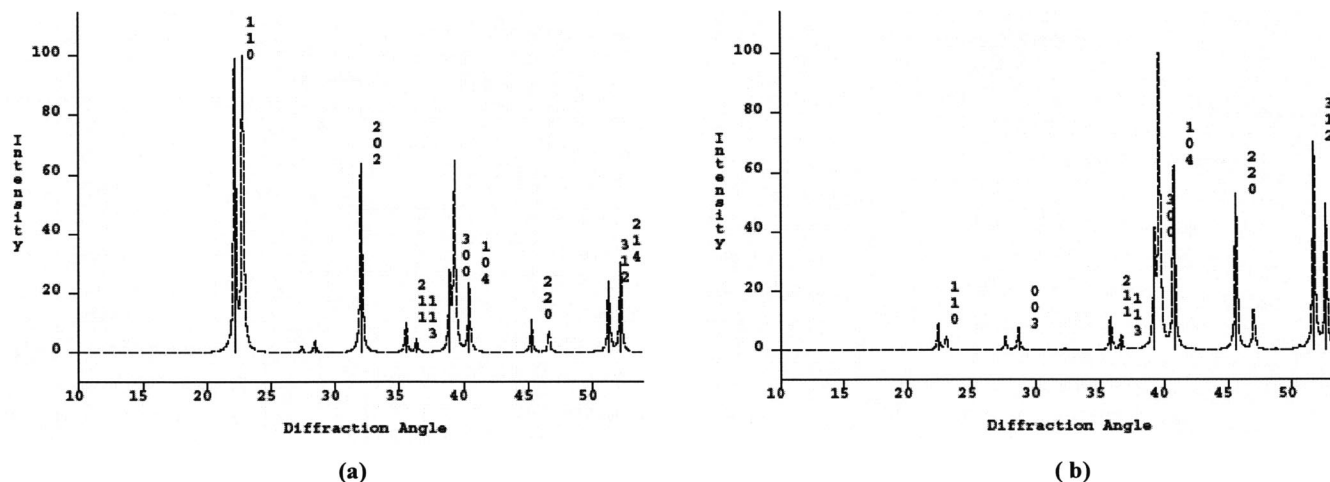


FIG. 6. Simulated x-ray and neutron diffractions from $R\text{-}3 \text{ Li}_3\text{AlH}_6$ using a Cu radiation of 1.542 \AA and a neutron source of 1.555 \AA , respectively: (a) XRD and (b) ND. Diffraction angles are 2θ values.

which agree well with experimental lattice parameters⁹ at around 440 K

$$a = 7.9 \text{ \AA}, \quad b = 8.1 \text{ \AA}, \quad c = 5.7 \text{ \AA}$$

$$\text{with } \alpha = 90.0^\circ, \quad \beta = 91.9^\circ, \quad \gamma = 90.0^\circ,$$

$$\rho = 0.994 \text{ g cm}^{-3}.$$

We also perform full optimizations to calculate the geometries and atomic positions for the hexagonal structure [see Fig. 5(c)]. Brink and Hauback²⁹ have recently reported that their Li_3AlD_6 structure at 295 K has the hexagonal symmetry corresponding to space group of No. 148. We find that the simulated ND hkl patterns [see Fig. 6(b)] from this structure agree well with their experimental data. The simulated strongest two ND reflections from this hexagonal structure are (032) with $2\theta = 45.72^\circ$ and (230) with $2\theta = 45.95^\circ$ and $I(230)/I(032) = 99.5\%$, the third strongest peak (33-3) with $2\theta = 71.44^\circ$ and $I(33-3)/I(032) = 72.47\%$, and the fourth strongest peak (202) with $2\theta = 39.68^\circ$ and $I(202)/I(032) = 62.39\%$. In addition we find that the calculated energy per formula unit at 0 K is more stable than that for the monoclinic Li_3AlH_6 structure. Next, we remove the symmetry constraints corresponding to space groups $P2_1/m$ and $R\text{-}3$ and then perform molecular dynamic simulations to see how the energies can change as the temperature increases. We find that at 295 K the structure having originally been in a monoclinic symmetry is 1.6 kcal/mol per formula unit higher than that in a hexagonal symmetry, but it becomes more stable by 3.3 kcal/mol per formula unit at 439 K. Consequently, these

results appear to support two experimental findings in given above, that is, at 295 K the most stable phase for Li_3AlH_6 is for the hexagonal structure (space group $R\text{-}3$) as shown by Brink *et al.*, but at 495 K the most stable phase is for the monoclinic structure (space group $P2_1/m$) as shown by Chen *et al.* The simulated XRDs at 295 K and 493 K are also consistent with the experimental data. However, our calculations show that the XRD peaks from Chen *et al.* could not be reproduced from their proposed structure with $P2_1/m$ symmetry as shown in Fig. 5(a).

D. LiH and LiAlH

Figure 7(c) shows the LiH structure of the “NaCl” type. This structure can be thought of as Li^+ ions stabilizing H^- anions and has predicted lattice parameters

$$a = b = c = 8.05 \text{ \AA} \quad \text{with } \alpha = \beta = \gamma = 90.0^\circ.$$

These parameters compare to the experimental data²⁹

$$a = b = c = 8.13 \text{ \AA} \quad \text{with } \alpha = \beta = \gamma = 90.0^\circ.$$

Figure 7(b) also shows the predicted structure for LiAlH , which is considered as a rhombohedra distortion of B32 LiAl with a shift of Li atoms by 0.1 \AA . The predicted lattice parameters (0 K) are

$$a = 7.1 \text{ \AA}, \quad b = c = 6.1 \text{ \AA} \quad \text{with } \alpha = \beta = \gamma = 90.0^\circ.$$

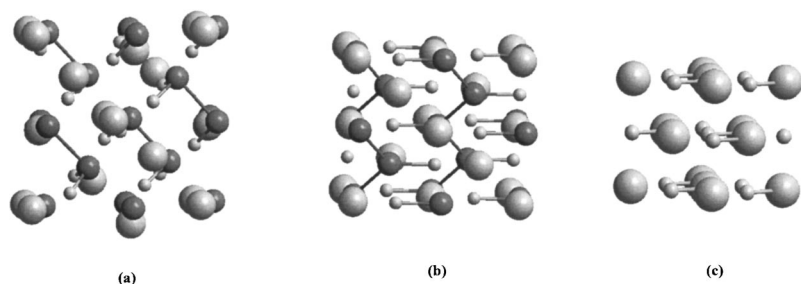


FIG. 7. Optimized structures for dihydride and monohydride intermediates: (a) LiAlH_2 , (b) LiAlH , and (c) LiH. Li and H atoms in gray are shown in large and small spheres, respectively, while Al atoms are shown in dark gray.

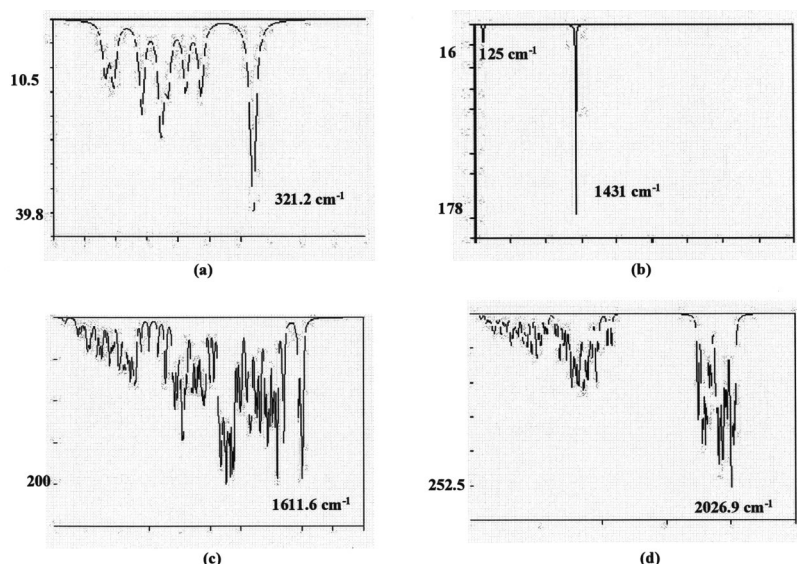


FIG. 8. Vibration spectra for the most stable phases: (a) LiAl, (b) LiH, (c) Li₃AlH₆, and (d) LiAlH₄.

E. Vibration frequencies

The vibration frequencies are necessary to determine zero-point corrections and the temperature dependence of the thermodynamic properties.³⁰ In addition it is useful for investigating such properties as thermal expansion and thermal conductivity. Figure 8 shows the vibration spectra calculated from the most stable phases of LiAl, LiH, Li₃AlH₆, and LiAlH₄ compounds.

F. Dehydriding reactions

Table I summarizes the thermodynamic stabilities for decomposition reactions. First, thermal decomposition of LiAlH₄ can occur through the two possible reactions:



Chen *et al.*⁹ showed that the first reaction proceeds around 165 °C and it liberates 5.3 wt. % of hydrogen. We predict the first reaction to be endothermic by 14.1 kcal/mol, while the second reaction is endothermic by 17.4 kcal/mol. We also determine the Gibbs free energy at 298 K for the first reac-

tion and find that the predicted value of 6.9 kcal/mol is in a close agreement with 6.6 kcal/mol by Dymova *et al.*³¹ In addition the reaction pathway connecting LiAlH₄ to Li₃AlH₆ is determined at the KMLYP/6-31+*G(d,p)* level of theory. The phase of Eq. 1 occurs through a five-step mechanism as shown in Fig. 9. The first and second steps of this decomposition are conversion of three LiAlH₄ molecules to one Li₃AlH₆ plus two AlH₃ molecules, which occur through the stepwise mechanism involving two sequential hydrogen transfers as shown in Figs. 9(a)–9(e). We find the first hydrogen transfer of this sequential reaction to proceed with an activation barrier of 8.6 kcal/mol (without zero-point corrections) and the formation of a five H coordinated Al intermediate to be endothermic by 0.2 kcal/mol. Then, the second H migrates from LiAlH₄ to this five H coordinated Al, which eventually produces one Li₃AlH₆ and two AlH₃ as shown in Fig. 9(e). We calculate the barrier of this reaction to be 8.1 kcal/mol relative to the LiAlH₄. Therefore, the overall activation barrier per formula unit relative to the initial LiAlH₄ structure calculated at the KMLYP/6-31+*G(d,p)* level of theory is 8.6 kcal/mol and the formation of one Li₃AlH₆ plus two AlH₃ is endothermic by 4.2 kcal/mol. The next three

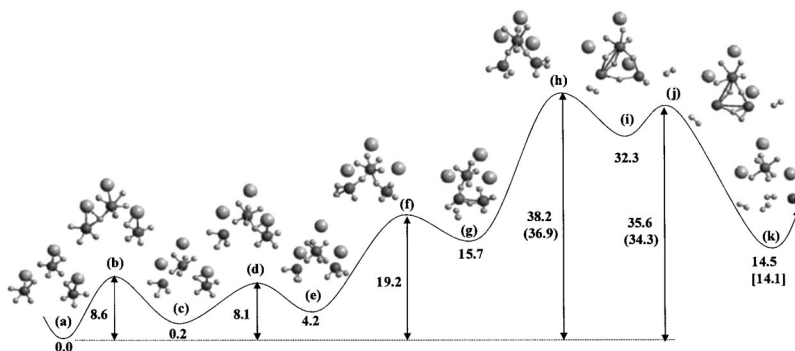


FIG. 9. Reaction energies for decomposition mechanism of LiAlH₄ to Li₃AlH₆: (a) the initial LiAlH₄, (b) the transition state of the first decomposition, (c) the intermediate with one AlH₃ generated, (d) the transition state of the second decomposition, (e) the intermediate with two AlH₃ and one Li₃AlH₆ generated, (f) the transition state for the first H₂ desorption, (g) the intermediate with one H₂ generated, (h) the transition state for the second H₂ desorption, (i) the intermediate with two H₂ generated, (j) the transition state for the third H₂ desorption, and (k) the final Li₃AlH₆ with Al and H₂ molecules generated. Li and H atoms in gray are shown in large and small spheres, respectively, while Al atoms are shown in dark gray. Energies are in kcal/mol. Not to scale.

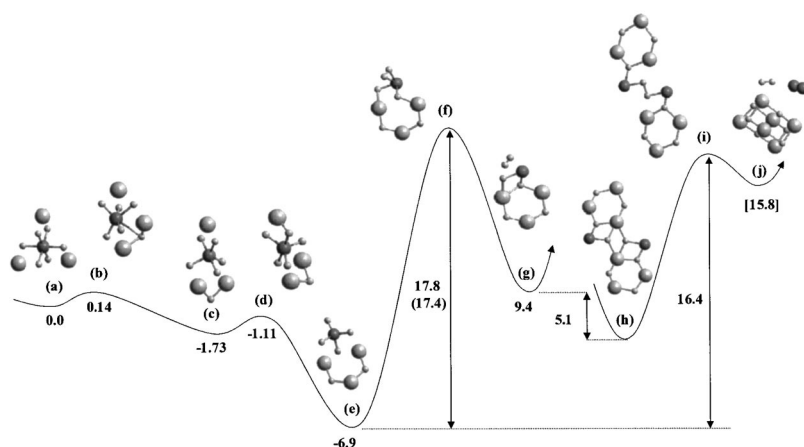


FIG. 10. Reaction energies for decomposition mechanism of Li₃AlH₆ to LiH: (a) the initial Li₃AlH₆, (b) the transition state of the first decomposition, (c) the one H-bridged intermediate generated, (d) the transition state of the second decomposition, (e) the two H-bridged intermediate, (f) the transition state for the first H₂ desorption, (g) the four H-bridged intermediate, (h) the eight H-bridged intermediate, (i) the transition state for the second H₂ desorption, and (j) the final LiH with Al and H₂ molecules generated. Li and H atoms in gray are shown in large and small spheres, respectively, while Al atoms are shown in dark gray. Energies are in kcal/mol. Not to scale.

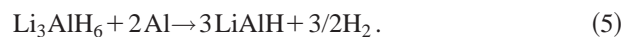
steps connecting LiAlH₄ to Li₃AlH₆ further convert one Li₃AlH₆ plus two AlH₃ to one Li₃AlH₆ plus two Al and three H₂ as shown in Figs. 9(e)–9(k). The first step to form the H-bridged intermediate plus one H₂ desorbed [Fig. 9(e)] proceed with an overall activation barrier of 19.2 kcal/mol and endothermic by 15.7 kcal/mol per formula unit relative to the initial LiAlH₄. Then, H₂ desorbs to produce another H-bridged intermediate as shown in Fig. 9(i). We find an activation barrier of 38.2 kcal/mol per formula unit relative to the LiAlH₄, which reduces to 36.9 kcal/mol with zero-point corrections. Next, the bridged H bonds to its neighboring hydrogen atom to produce another H₂. This H₂ desorption proceeds with an activation barrier of 34.3 kcal/mol with respect to the initial LiAlH₄. Consequently, these five reaction steps produce three H₂ and two Al plus one Li₃AlH₆ from three LiAlH₄. Thus, using the computed partition functions for the reactants and the transition state the reaction rate k of the canonical rate equation³² is determined by

$$k = \Gamma(T) \frac{k_B T}{h} \frac{Q_{TS}}{Q_A Q_B} \exp\left(\frac{-\Delta E_0}{k_B T}\right), \quad (3)$$

where $\Gamma(T)$ is the thermal tunneling coefficient which can be obtained by the same scheme in the work of the previous study,¹⁶ Q_{TS} is the partition functional for the transition state, Q_A and Q_B are the partition functions for the reactants A and B, respectively, and ΔE_0 is the barrier height. The resulting dependence of solid state transformation from LiAlH₄ to Li₃AlH₆ on temperature is given by $k = 1.76 \times 10^{12} \exp(-36900/RT)$ where R is in units of 1.987/K. Since the phase transition of Eq. 1 occurs through solid-state decomposition, one would expect that the phase transition from LiAlH₄ to Li₃AlH₆, takes place locally. Thus after decomposition the resulting material ought to be a rather homogeneous mixture of extremely small domains for each phase. However, the diffraction experiments⁹ show narrow peaks for product phases, indicating that these phases were present as relatively large crystallites, implying that there must be some long-range mechanism transporting metal species to the sites where crystallites are formed. Thus in decomposition of LiAlH₄, Al must be transported toward the growing Al crystallites. We find that the resulting reaction for Eq. 1 is endothermic by 14.5 kcal/mol at the KMLYP/6-31 + G(d,p) level of theory, which is also consistent with 14.1

kcal/mol at the PW91 method using the cutoff energy of 270 eV. How this transport occurs and what role the catalysts play are not known at this point. Our calculated 14.1 kcal/mol enthalpy for Eq. 1 suggests that the phase transformation of $P2_1/c$ LiAlH₄ to $R-3$ Li₃AlH₆ could also occur via the intermediate phases of $Pnma$ LiAlH₄ and $Pm-3m$ LiAlH₄. Vajeeston *et al.*¹⁰ have recently shown that $P2_1/c$ transforms to $Pnma$ LiAlH₄ at 33.8 GPa. However, it is still unclear whether the phase transformations of $Pnma$ LiAlH₄ through $Pm-3m$ LiAlH₄ to $R-3$ Li₃AlH₆ are induced at moderate pressures. Consequently we encourage the further detailed study to know how the pressure-induced reaction mechanism may differ from our proposed temperature-induced reaction mechanism of LiAlH₄ to Li₃AlH₆.

Next, thermal decomposition of Li₃AlH₆ can occur via the two possible reactions as



The first reaction proceeds around 195 °C, and it liberates 2.6 wt. % of hydrogen. The first reaction is predicted to proceed through a four-step mechanism as shown in Fig. 10. In the first step, two Li atoms accept one H to form a stable H-bridged intermediate [see Fig. 10(c)] from AlH₆. Likewise, in the second step, three Li also play a critical role to stabilize the second H atom transferred from AlH₅ by forming another H-bridged intermediate as shown in Fig. 10(e), which is exothermic by 6.18 kcal/mol per formula unit relative to the Li₃AlH₆. Then, the H₂ desorption occurs through the transition state [Fig. 10(f)] to form the third H-bridged intermediate structure [Fig. 10(g)]. This reaction is predicted to have an activation barrier of 17.8 kcal/mol at the KMLYP/6-31 + G method, which reduced to 17.4 kcal/mol with zero-point corrections and is a rate-limiting step. As a result, the rate of solid state transformation from Li₃AlH₆ to LiH is given by $k = 5.72 \times 10^{12} \exp(-17400/RT)$. Finally, the H bridge intermediates combine to form one H₂ plus two Al and six LiH molecules, which eventually can form fcc Al and fcc LiH plus hydrogen. We predict that the resulting reaction is endothermic by 15.8 kcal/mol without zero-point corrections, which compares to the experimentally proposed enthalpies of 9.8 kcal/mol⁹ and 23.9 kcal/mol.³³ On the other

hand, we predict the second reaction to be endothermic by 57.2 kcal/mol (without zero-point corrections). Consequently, our calculations suggest that decomposition of Li_3AlH_6 would preferentially occur through the reaction 4.

Dehydriding of LiH through phase-separated B32 LiAl is predicted to be energetically favorable to decomposition though LiH and Al.



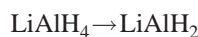
IV. SUMMARY AND CONCLUSIONS

We used density functional theory and x-ray and neutron diffraction methods to investigate the reaction mechanisms as well as the crystal structures, atomic configurations, and vibration frequencies of various possible intermediate structures for hydrogen storage based on LiAl hydride systems. Particular attention was paid to three consecutive decomposition reactions involved in dehydriding of LiAlH_4 . First, we determined the crystal structures for various compounds, including LiAl, LiAlH_4 , Li_3AlH_6 , LiAlH_2 , LiAlH, LiH, and Al. In each case we explored several plausible structures and determined the lowest energy form. For LiAlH_4 and Li_3AlH_6 there were reported XRD patterns and we find that our structures agree well with the intensities in these patterns, in addition to agreeing with the overall lattice parameters and densities. Thus we consider that we have now established the stable crystalline structures for these systems.

We also considered decomposition of LiAlH_4 into the various phases. We predict that decomposition



while the alternative reaction



Thus we agree with the conclusion of the experiments that decomposition of LiAlH_4 leads to formation of Li_3AlH_6 . This reaction is found to proceed through a five-step mechanism with an overall activation barrier of 36.9 kcal/mol. The first and second steps convert three LiAlH_4 molecules to one Li_3AlH_6 plus two AlH_3 molecules, occurring through two sequential hydrogen transfers with an overall barrier of 8.6 kcal/mol. The third, fourth, and fifth steps connecting LiAlH_4 to Li_3AlH_6 further convert one Li_3AlH_6 plus two AlH_3 to one Li_3AlH_6 plus two Al and three H_2 , occurring with an activation barrier of 38.2 kcal/mol per formula unit relative to the LiAlH_4 , which reduces to 36.9 kcal/mol with zero-point corrections. Next, we examined the thermal decomposition mechanism of Li_3AlH_6 into fcc LiH with a simultaneous phase separation of fcc Al, which occurs through a four-step mechanism with an activation barrier of 17.4 kcal/mol for the rate-limiting step. In the first and second steps two Li atoms accept two H atoms to form H bridged intermediate from AlH_6 . Then, two sequential H_2 desorption steps are followed, which result in fcc LiH plus Al and H_2 as



We calculate that this reaction is endothermic by 15.8 kcal/mol, and find that this dissociation energy compares to the experimental enthalpies of 9.8–23.9 kcal/mol. Finally, we explore thermal decomposition of LiH,



We find that the lowest energy structure for LiAl is for the B32 phase. Additionally, we examined alternative structure for the phases involved in these steps.

ACKNOWLEDGMENTS

This research was supported by General Motors Global Alternative Proposal Center (GM GAPC). The computational resources at the Materials and Process Simulation Center (MSC) in California Institute of Technology and Korea Advanced Institute of Science and Technology have been supported by grants from NSF-MRI, ARO-DURIP, and by a SUR grant from IBM. The authors would like to acknowledge the support from KISTI (Korea Institute of Science and Technology Information) under “the 5th Strategic Supercomputing Applications Support Program” with Dr. S. M. Lee as the technical supporter. The use of the computing system of the Supercomputing Center is also greatly appreciated.

¹L. Schlappbach and A. Züttel, *Nature (London)* **414**, 353 (2001).

²J. Pettersson and O. Hjortsberg, *Hydrogen Storage Alternatives: A Technological and Economic Assessment* (KFB-Deddelande 1999:27), <http://www.kfb.se/pdf/M-99-27.pdf>

³D. Hart, *Storing and Transporting Hydrogen*, E-sources (1998), <http://www.esources.com/hydrogen/storage.html>

⁴A. C. Dillon, K. M. Jones, T. A. Bekkedahl, C. H. Kiang, D. S. Bethune, and M. J. Heben, *Nature (London)* **386**, 377 (1997).

⁵M. Hirscher, M. Becher, M. Haluska *et al.*, *Appl. Phys. A: Mater. Sci. Process.* **72**, 129 (2001).

⁶P. Chen, X. Wu, J. Lin, and K. L. Tan, *Science* **285**, 91 (1999).

⁷G. D. Berry and S. M. Aceves, *Energy Fuels* **12**, 49 (1998).

⁸A. T.-Raissi, A. Banerjee, and K. Sheinkopf, *Proceedings of the 31st Inter-society Energy Conversion Engineering Conference*, 1996.

⁹J. Chen, N. Kuriyama, Q. Xu, H. T. Takeshita, and T. Sakai, *J. Phys. Chem. B* **105**, 11214 (2001).

¹⁰P. Vajeeston, P. Ravindran, R. Vidya, H. Fjellvåg, and A. Kjekshus, *Phys. Rev. B* **68**, 212101 (2003).

¹¹P. Vajeeston, P. Ravindran, A. Kjekshus, and H. Fjellvåg, *Phys. Rev. B* **69**, 020104 (2004).

¹²P. E. Blöchl, *Phys. Rev. B* **50**, 17953 (1994).

¹³P. Hohenberg and W. Kohn, *Phys. Rev.* **136**, B864 (1964).

¹⁴W. Kohn and L. J. Sham, *Phys. Rev.* **140**, A1133 (1965).

¹⁵J. P. Perdew and Y. Wang, *Phys. Rev. B* **45**, 13244 (1992).

¹⁶J. K. Kang and C. B. Musgrave, *J. Chem. Phys.* **115**, 11040 (2001).

¹⁷D. Vanderbilt, *Phys. Rev. B* **41**, 7892 (1990).

¹⁸H. J. Monkhorst and J. D. Pack, *Phys. Rev. B* **13**, 5188 (1976).

¹⁹M. J. Gillan, *J. Phys.: Condens. Matter* **1**, 689 (1989).

²⁰M. C. Payne, M. P. Teter, D. C. Allan, T. A. Arias, and J. D. Joannopoulos, *Rev. Mod. Phys.* **64**, 1045 (1992).

²¹B. Delley, *J. Chem. Phys.* **92**, 508 (1990).

²²M. J. Frisch, G. W. Trucks, H. B. Schlegel *et al.*, *GAUSSIAN03* (Gaussian Inc., Pittsburgh, PA, 2003).

²³M. J. Frisch, J. A. Pople, and J. S. Binkley, *J. Chem. Phys.* **80**, 3265 (1984).

²⁴A. J. Howard, G. L. Gilliland, B. C. Finzel, T. L. Poulos, D. H. Ohlendorf, and F. R. Salemme, *J. Appl. Crystallogr.* **20**, 383 (1987).

²⁵M. M. J. Treacy, J. M. Newsam, and M. W. Deem, *Proc. R. Soc. London, Ser. A* **443**, 499 (1991).

- ²⁶See EPAPS Document No. E-JCPSA6-121-510439 for a complete list of optimized structural parameters and energies for LiAl , LiAlH_4 , Li_3AlH_6 , LiAlH_2 , LiAlH , LiH , Al compounds, and H_2 molecule. Simulated powder x-ray and neutron diffraction results for $P2_1/c$ LiAlH_4 and $P2/m$ Li_3AlH_6 from this work are also available. A direct link to this document may be found in the online article's HTML reference section. The document may also be reached via the EPAPS homepage (<http://www.aip.org/pubservs/epaps.html>) or from <ftp.aip.org> in the directory /epaps/. See the EPAPS homepage for more information.
- ²⁷I. Barin, O. Knacke, and O. Kubaschewski, *Thermochemical Properties of Inorganic Substances* (Springer, Berlin, 1977).
- ²⁸X.-Q. Guo, R. Podlucky, and A. J. Freeman, *Phys. Rev. B* **40**, 2793 (1989).
- ²⁹B. C. Hauback, H. W. Brinks, and H. Fjellvåg, *J. Alloys Compd.* **346**, 184 (2002).
- ³⁰H. W. Brinks and B. C. Hauback, *J. Alloys Compd.* **354**, 143 (2003).
- ³¹T. N. Dymova, D. P. Aleksandrov, V. N. Konoplev, T. A. Silina, and A. S. Sizareva, *Russ. J. Coord. Chem.* **20**, 263 (1994).
- ³²S. Glasstone, K. Laidler, and H. Eyring, *The Theory of Rate Processes* (McGraw-Hill, New York, 1941), Chaps. 1 and 4.
- ³³V. I. Mikheeva and S. M. Arkhipov, *Russ. J. Inorg. Chem.* **12**, 1066 (1967).